

Enhanced Formic Acid Oxidation over SnO₂-decorated Pd Nanocubes

Clara Rettenmaier, Rosa M. Arán-Ais, Janis Timoshenko, Rubén Rizo, Hyo Sang Jeon, Stefanie Kühn, See Wee Chee, Arno Bergmann, and Beatriz Roldan Cuenya*

Cite This: *ACS Catal.* 2020, 10, 14540–14551

Read Online

ACCESS |

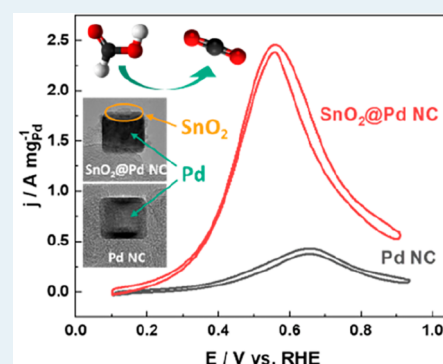
Metrics & More

Article Recommendations

Supporting Information

ABSTRACT: The formic acid oxidation reaction (FAOR) is one of the key reactions that can be used at the anode of low-temperature liquid fuel cells. To allow the knowledge-driven development of improved catalysts, it is necessary to deeply understand the fundamental aspects of the FAOR, which can be ideally achieved by investigating highly active model catalysts. Here, we studied SnO₂-decorated Pd nanocubes (NCs) exhibiting excellent electrocatalytic performance for formic acid oxidation in acidic medium with a SnO₂ promotion that boosts the catalytic activity by a factor of 5.8, compared to pure Pd NCs, exhibiting values of 2.46 A mg⁻¹_{Pd} for SnO₂@Pd NCs versus 0.42 A mg⁻¹_{Pd} for the Pd NCs and a 100 mV lower peak potential. By using ex situ, quasi in situ, and operando spectroscopic and microscopic methods (namely, transmission electron microscopy, X-ray photoelectron spectroscopy, and X-ray absorption fine-structure spectroscopy), we identified that the initially well-defined SnO₂-decorated Pd nanocubes maintain their structure and composition throughout FAOR. In situ Fourier-transformed infrared spectroscopy revealed a weaker CO adsorption site in the case of the SnO₂-decorated Pd NCs, compared to the monometallic Pd NCs, enabling a bifunctional reaction mechanism. Therein, SnO₂ provides oxygen species to the Pd surface at low overpotentials, promoting the oxidation of the poisoning CO intermediate and, thus, improving the catalytic performance of Pd. Our SnO_x-decorated Pd nanocubes allowed deeper insight into the mechanism of FAOR and hold promise for possible applications in direct formic acid fuel cells.

KEYWORDS: formic acid oxidation, Pd, Sn, nanocubes, in situ FTIR, quasi in situ XPS, operando XAFS



1. INTRODUCTION

Fuel cells are efficient power sources that generate electric energy from chemical reactions.¹ Among the low-temperature fuel cells, the direct formic acid fuel cell (DFAFC) has attracted significant attention since the 1960s,^{2–4} because of the high electromotive force (1.45 V) and low fuel crossover.⁵ The benefit of formic acid as a fuel source is based on its safety, low toxicity, and its straightforward synthesis from abundant natural biomass.¹ Moreover, the formic acid oxidation reaction (FAOR) serves as a model system for a structure-sensitive, two-electron-transfer electrochemical reaction,⁶ of which fundamental understanding can serve to elucidate more-complex processes.

FAOR proceeds through a widely accepted dual-path mechanism. In the direct pathway, CO₂ is produced through an active intermediate of unclear nature, while in the indirect pathway, the formation of the poisoning intermediate HCOO_{ads}/CO_{ads} occurs through dehydration.^{2,4,7,8} Extensive studies have shown that the direct pathway is more favorable on Pd than on Pt.^{9–11} The less favorable poisoning by CO and lower FAOR onset potential for Pd, compared to Pt, leads to an enhanced initial catalytic performance of Pd-containing systems.^{4,9,12} However, it is also widely accepted that Pd still

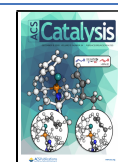
suffers from slow deactivation through the adsorption of poisoning CO_{ads}.^{11,13}

The structure sensitivity of FAOR has been systematically explored using Pd single crystals,^{14,15} as well as shape-controlled (and thus facet-oriented) Pd nanoparticles (NPs).^{16,17} Particularly, the {100} orientation exhibits the highest FAOR performance of all basal planes, which was explained by its capacity to stabilize two bridge formate species as compared to other facets.^{15–19} In this respect, cubic NPs are enclosed by six {100} facets in bulk face-centered cubic (fcc) structures, making these nanostructures perfect model systems for studying FAOR. However, a limitation of the shaped NPs is their morphological instability.^{20,21} It has been reported that monometallic Pd catalysts deactivate and degrade by dissolution of Pd under acidic operation conditions,^{13,22,23} and, thus, the preservation and optimization of the activity and

Received: July 23, 2020

Revised: October 23, 2020

Published: November 25, 2020



stability of the catalyst is of crucial interest. Therefore, the addition of a second metal, such as Au,^{22,23} Pt,²⁴ Ag,²⁵ Ti,²⁶ Pb,²⁷ Fe,²⁸ or Sn,^{1,5,29–35} provides a common strategy for enhancing the activity and stability of Pd-based catalysts. Most known Pd-M catalysts form alloys, which not only lead to a variation of the reaction mechanism, but also generally improve the stability.³⁶

A few examples of the use of Pd–Sn systems for FAOR applications have been previously reported, all demonstrating that CO oxidizes more easily on the Sn-containing samples, leading to an improved catalytic activity for FAOR.^{29–34} The particular interest in Sn arises from its ability to oxidize potentially poisoning intermediates such as CO on Pd or Pt at low overpotentials, through an electronic effect,^{29,30,37} a bifunctional mechanism,^{32,38} or a third-body effect.^{9,39,40} Regarding the electronic effect, alloying Sn with Pd modifies the electronic structure of the catalyst, lowering the adsorption energy of the intermediates. In fact, the increased catalytic performance of alloyed PdSn/C NPs, prepared via a microwave-assisted polyol method, was assigned to an expansion of the lattice parameter of Pd and, thus, to a modified electronic structure.^{29,30} Regarding the bifunctional mechanism, the presence of oxidized Sn species was found to facilitate the CO oxidation and, hence, increase the FAOR activity,^{32,38} while it also improved its stability.⁵ In particular, PdSn–SnO₂ catalysts with different degrees of interfacial contact have demonstrated substantially lower CO poisoning and higher catalytic activity, compared to alloyed PdSn catalysts.³¹ The third-body effect, in turn, is defined by the inhibition of possible CO_{ads} adsorption sites through adatoms or steric hindrance, thereby facilitating the adsorption of formic acid.^{9,39,40}

Therefore, SnO_x decoration is a promising approach to increase the catalytic activity, but it is not yet clear how SnO_x interacts with the most active Pd{100} surface, particularly under FAOR conditions, and whether the reaction pathway is modified. Furthermore, FAOR on Pd electrocatalysts has rarely been studied with spectroscopic methods under reaction conditions, although the few existing in situ FTIR studies reveal interesting mechanistic aspects. For example, the dependence of the CO_{ad} coverage on the CO₂ concentration at the surface was observed, leading to the conclusion that the origin of CO_{ad} could be the reduction of the product CO₂ over the Pd surface.^{9,41–43}

In the present study, we report a comparison of SnO₂-decorated Pd (SnO₂@Pd) NCs and monometallic Pd NCs with a preferential Pd{100} surface structure, prepared via a hydrothermal synthesis route and supported on carbon. Spectroscopic and microscopic characterization of the SnO₂@Pd catalysts revealed a cubic Pd core with an incomplete SnO₂ outer shell, which remains in close contact with Pd during the reaction. Quasi in situ X-ray photoelectron spectroscopy (XPS) and operando X-ray absorption fine-structure (XAS) spectroscopy data revealed that the Sn⁴⁺ oxidation state is preserved under reaction conditions, while in situ Fourier-transform infrared (FTIR) spectroscopy suggested the presence of a weaker CO adsorption site on Pd. We found that the addition of SnO₂ improves the catalytic activity of Pd NCs toward FAOR in acidic media, because it leads to a decrease in the oxidizing potential of CO intermediates, keeping the active Pd sites free of poisoning intermediates.

2. EXPERIMENTAL SECTION

2.1. Synthesis of Pd and SnO₂@Pd Nanocubes. Pd nanocubes were prepared through a hydrothermal synthesis route by modifying a previously reported method.¹⁸ Dihydrogen tetrachloropalladate (H₂PdCl₄, 10 mM) was prepared from 10 mM PdCl₂ (99.9%, Sigma–Aldrich) and 20 mM HCl (ACS reagent, 37%, Sigma–Aldrich) and reduced by L-ascorbic acid (99%, Alfa Aesar) under the presence of hexacetyltrimethylammonium bromide (CTAB, >99%, Sigma–Aldrich) at 95 °C. After 25 min, the solution was centrifuged, washed two times with 1:1 ethanol/water, and dispersed in ultrapure water (resistance = 18.2 MΩ). The SnO₂@Pd NCs were prepared by following the same method and with further addition of 5 at.% SnSO₄ (>95%, Sigma–Aldrich) 15 min after the start of the reaction. The NCs were supported on carbon by adding carbon Vulcan XC72R powder to the nanocubes' aqueous dispersion and sonicating the suspension thoroughly. The ligands were removed by adding 0.25 M NaOH. After complete precipitation, the samples were washed thoroughly with ultrapure water and dried at 105 °C overnight.

The catalyst inks with a concentration of 4 mg/mL were prepared by sonicating the carbon-supported NCs in isopropanol for 5 min. From this, a 10-μL aliquot, corresponding to 40 μg of catalyst, was pipetted onto a glassy carbon substrate and dried in air.

2.2. Electrochemical Measurements. Electrochemical characterization was performed in Ar-saturated 0.5 M H₂SO₄ (95%, VWR). FAOR was studied in an Ar-saturated 0.1 M HClO₄ (70%, 99.999% trace metal basis, Sigma–Aldrich) containing 0.5 M HCOOH (96%, Sigma–Aldrich) in a three-electrode electrochemical cell at 50 mV s⁻¹ using a Biologic SP300 potentiostat. A reversible hydrogen electrode (RHE) (HydroFlex, Gaskatel) and a leak-free Ag/AgCl (LF-1, Innovative Instruments Inc., 3.4 M KCl) were used as reference electrodes. Au wire served as a counter electrode. The catalyst-covered glassy carbon electrode was immersed into the solution with a hanging meniscus configuration. Before each experiment, the catalysts were activated by cycling 10 times in 0.1 M HClO₄ between 0.1 and 0.7 V at 50 mV s⁻¹. The collected electrochemical data were IR-corrected, and the ohmic drop was obtained based on *i*-interrupt or impedance measurements. In addition, the data were normalized by the Pd mass of each catalyst obtained by inductively coupled plasma mass spectrometry (ICP-MS). All potential scales were converted to RHE. CO-stripping experiments were performed by dosing CO (Westfalen, 3.7) into the electrolyte while holding the potential of the working electrode at 0.15 V until total surface inhibition, which was monitored by cyclic voltammetry between 0.1 V and 0.4 V through the disappearance of the H_{Ads/Des} peaks. The residual CO in the electrolyte was removed by purging with Ar for 15 min. The adsorbed CO was completely stripped off the surface through a cyclic voltammogram up to 1.0 V at 20 mV s⁻¹. The second cycle shows the reappearance of the H_{upd} adsorption and desorption peaks, which disappeared during the CO_{ads} blockage. Chronoamperometric measurements were performed by holding the working potential at 0.1 V for 10 s, where no reaction occurs, and at 0.45 V for 180 min. Tafel slopes were calculated in a quasi-steady state from forward linear sweep voltammograms at 1 mV s⁻¹.

The electrochemical surface area (ECSA) was evaluated from the H_{des} peak after CO-stripping experiments and by the area of the CO oxidation features. For H_{des} , the values were calculated by integrating the CVs between 0.11 V and 0.42 V and normalizing by the theoretical charge ($Q_{\text{H}} = 210 \mu\text{C cm}^{-2}$ for a one-electron transfer per Pd atom.⁴⁴ The surface area through CO oxidation was obtained by integrating the CVs between 0.75 V and 1.0 V with the blank CV as a baseline and normalizing by $Q_{\text{CO}} = 420 \mu\text{C cm}^{-2}$ for a two-electron transfer per Pd atom.⁴⁵

2.3. Inductively Coupled Plasma–Mass Spectrometry (ICP-MS). The compositions of the catalysts, based on atomic percentage and weight percentage, were determined by inductively coupled plasma–mass spectrometry (ICP-MS) (Thermo Fisher iCAP RQ). The digestion of the samples was performed by adding a mixture of acids (1:1:3 $\text{H}_2\text{SO}_4:\text{HNO}_3:\text{HCl}$) into a known amount of the catalyst and heating to 180 °C for 30 min, using the digestion Microwave Multiwave GO from Anton Paar. The solution was then filtered to remove any remaining carbon residues and then diluted 100 times in 3% HCl. The electrolyte was diluted 3.33 times in 3% HCl.

2.4. Transmission Electron Microscopy (TEM) and Energy-Dispersive X-ray Spectroscopy (EDX). Transmission electron microscopy (TEM) and energy-dispersive X-ray spectroscopy (EDX) have been employed to investigate the morphology, size distribution, and local elemental composition of the catalysts. The measurements were performed with a FEI Talos F200X microscope equipped with a XFEG field-emission gun with an acceleration voltage of 200 kV, a scanning transmission electron microscopy (STEM) unit with a bright-field (BF) detector, two dark-field (DF) detectors, and a high-angle annular dark field (HAADF) detector, as well as SuperX 4 SDD EDX detector. The samples were prepared by placing a drop of a 4 mg/mL suspension in isopropanol on a Ni or Cu lacey carbon grid and allowing it to dry in air. For each sample, more than 200 nanocubes located on different parts of the grid were analysed to estimate the average size distribution. The composition of the NCs was analyzed via EDX, where maps were collected to analyze the elemental distribution. A schematic visualization of the obtained structure was made with VESTA.⁴⁶

2.5. X-ray Diffraction (XRD). X-ray diffraction (XRD) measurements were collected on a Bruker AXS D8 Advance diffractometer in Bragg–Brentano geometry. The setup employs Ni-filtered $\text{Cu K}\alpha_{1+2}$ radiation and a position-sensitive energy-dispersive LynxEye silicon strip detector. XRD patterns were measured in the range of 20° – 100° 2θ in continuous scanning mode, with an increment of 0.02° and a counting time of 1 s/step, which resulted in 185 s of total accumulation time per data point. The analysis of the diffraction patterns was performed with Rietveld refinements considering the instrumental broadening and sample displacement, using the software package TOPAS (Bruker-AXS).

2.6. Quasi In Situ X-ray Photoelectron Spectroscopy (XPS). XPS measurements were performed with a commercial Phoibos100 analyzer (SPECS GmbH, $E_{\text{pass}} = 15$ eV) and a XR50 (SPECS GmbH) X-ray source with an Al anode ($E_{\text{K}\alpha} = 1486.7$ eV). All spectra were aligned using Pd^0 (335.2 eV) as reference and fitted using a Shirley-type or a linear background subtraction for X-ray or Auger electron spectroscopy, respectively. Quasi in situ XPS experiments were performed while avoiding the exposure of the sample to air after the

electrochemical treatment. In this setup, an electrochemical cell is directly attached to the ultrahigh vacuum (UHV) system where the XPS chamber is located to allow the sample transfer without air exposure. The samples were first cycled between 0.1 V and 0.7 V in 0.1 M HClO_4 , then the reaction was performed after adding 0.5 M HCOOH to the electrolyte. Afterward, the samples were rinsed with deaerated ultrapure water and transferred to an ultrahigh vacuum (UHV) system in an Ar atmosphere. The electrochemical measurements were performed using a potentiostat (Autolab PGSTAT 302N).

2.7. Operando X-ray Absorption Fine-Structure Spectroscopy (Operando XAFS). XAFS measurements were performed at the undulator beamlines P64 and P65 of the PETRA III storage ring. A Si(311) double-crystal monochromator was used for energy selection, and an Rh-coated collimating mirror was used for the removal of higher harmonics and the reduction of the power load density on the monochromator. All experiments were conducted in fluorescence mode, using a passivated implanted planar silicon (PIPS) detector at the Pd K-edge (24350 eV) and Sn K-edge (29200 eV). The operando measurements were performed in a three-electrode electrochemical cell (see ref 47 for the schematics of the cell). A leak-free Ag/AgCl component was used as a reference electrode, while an Au wire was used as a counter electrode. The samples were prepared by drop casting 10 mg of catalyst on a 0.5 cm^2 area of carbon paper. Pd K-edge and Sn K-edge data were collected separately for identical fresh samples, to optimize the signal absorption edge and to avoid self-absorption. Carbon paper with the deposited catalyst served as a working electrode. It was mounted in the electrochemical cell and fixed with Kapton tape, so that the Kapton-covered carbon paper could act as X-ray window, while the side coated with the catalyst was in contact with the electrolyte. Measurements for both samples were performed in air as well as under operando conditions, in Ar-saturated 0.1 M HClO_4 + 0.5 M HCOOH solution. Energy calibration, background subtraction and normalization of the collected XAFS spectra were performed with the software Athena.⁴⁸ Details regarding the extended X-ray absorption fine-structure (EXAFS) fitting are summarized in [Supplementary Note 1](#) in the Supporting Information.

2.8. In situ Fourier-Transform Infrared Reflection Absorption (FTIR) Spectroscopy. In situ In situ FTIR data were acquired with a Vertex 80v spectrometer (Bruker) that was equipped with a MCT detector, using a thin layer configuration in the external reflection mode. An electrochemical cell was home-built around a CaF_2 IR window with a Au counter electrode and a leak-free Ag/AgCl reference electrode. A Au foil was chosen as the substrate for CO-stripping experiments to enhance the reflectivity (no CO adsorption was observed on the gold support in the potential range used). The electrode was transferred to the cell filled with an Ar-saturated 0.1 M HClO_4 electrolyte, CO was adsorbed under potential control, the remaining CO in the electrolyte was removed with Ar, and then the electrode was pressed against the CaF_2 window for the in situ FTIR measurements. For FAOR experiments, glassy carbon was used as a support; the amount of formic acid was reduced to 25 mM for better sensitivity of the onset potentials and to decrease the CO_2 bubble formation, which could displace the electrolyte in the thin-layer configuration. IR spectra were collected between 4000 cm^{-1} and 1000 cm^{-1} with 100 interferograms per spectrum and a spectral resolution of 4 cm^{-1} . Background

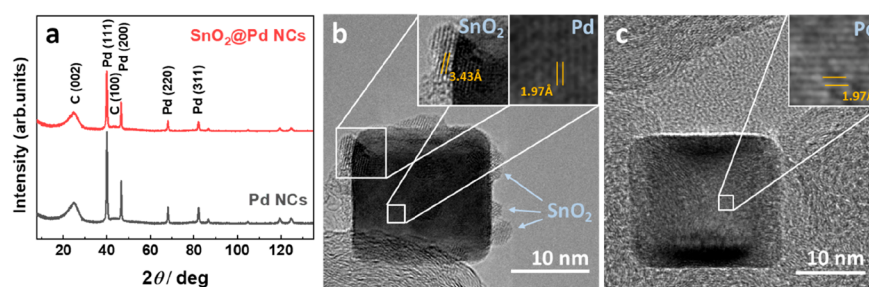


Figure 1. (a) XRD pattern of the as-prepared SnO_2 @Pd NC and Pd NC catalysts. High-resolution TEM images of (b) SnO_2 @Pd NCs and (c) Pd NCs supported on carbon powder.

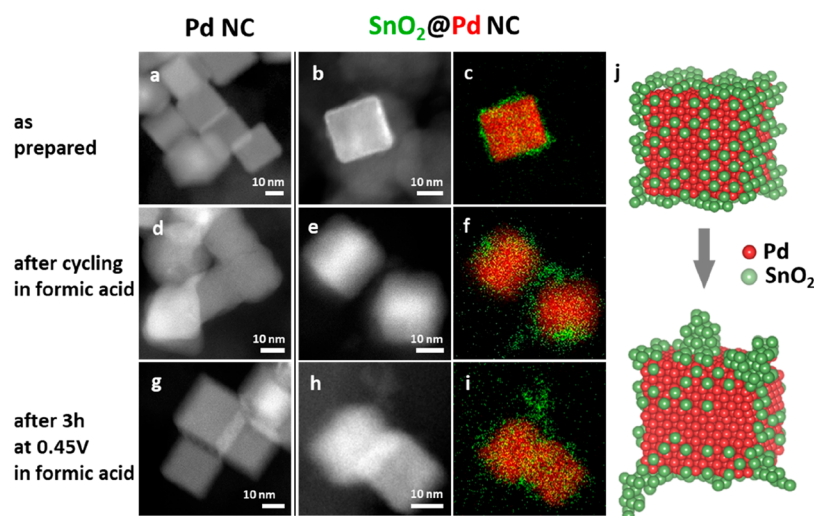


Figure 2. HAADF-STEM of Pd NCs (panels (a), (d), (g)) and SnO_2 @Pd NCs (panels (b), (e), (h)) with EDX mapping of SnO_2 @Pd NCs (panels (c), (f), (i)). TEM data of the as-prepared state of the samples are included in panels (a)–(c), those after cycling 10 times in FA are shown in panels (d)–(f), and those obtained after 3 h at 0.45 V in FA are shown in panels (g)–(i). The EDX maps of the SnO_2 @Pd NCs correspond to the same regions of the HAADF-STEM images shown. An model depicting the evolution of the structure and surface composition of the SnO_2 @Pd NC catalyst during FAOR is shown in panel (j). Sn atoms appear in green and Pd in red. The model representation is only for visual purposes, and it does not reflect the actual crystallographic size or atomic positions.

spectra were acquired at 0.06 V for CO stripping and -0.04 V for the FAOR experiments. The spectra are represented as absorbance, $A = -\log(R/R_0)$, where R and R_0 are the sample and reference reflectances, respectively. For CO-stripping and FAOR experiments, the background spectra were obtained after CO adsorption and after the addition of HCOOH, respectively. Thus, oxidation of CO is indicated by negative peaks for CO-stripping experiments, while CO_2 formation is indicated by a positive peak for both experiments.

3. RESULTS AND DISCUSSION

3.1. Catalyst Morphology and Structure Characterization. The crystalline structure, morphology, chemical composition, and distribution of the carbon-supported SnO_2 @Pd NCs and Pd NCs have been characterized by XRD (see Figure 1a, as well as Figure S1 in the Supporting Information), high-resolution TEM (Figures 1b and 1c), and STEM (see Figure 2, as well as Figures S2 and S3 in the Supporting Information). Moreover, the shape and the elemental distribution of both catalysts were tracked by high-angle annular dark-field scanning transmission electron microscopy (HAADF-STEM) and energy-dispersive X-ray spectroscopy (EDX) mapping in the as-prepared state, after cycling 20 times in the presence of formic acid and after 3 h of reaction at a constant working potential (see Figure 2, as well

as Figure S3). Cycling under oxidizing conditions was performed for testing the stability of the NCs in terms of morphology and chemical changes in the working potential range, while potentiostatic measurements were done to gain insight into the nanocubes' activity, stability, and resistance against CO poisoning.

Figure 1a shows XRD patterns of the as-prepared catalysts. Besides the broad (002) reflection of the hexagonal graphite structure of the carbon support, all other diffraction peaks can be assigned to the typical fcc Pd bulk structure. In the SnO_2 @Pd catalyst, the presence of crystalline Sn or a SnO_x phase is not observed, which indicates the absence of significant Sn agglomeration. Note here that the presence of small amounts of Sn species on Pd cannot be ruled out by XRD. Rietveld refinement of the XRD pattern revealed very similar Pd lattice parameters for both samples with 3.88959 ± 0.00012 Å for SnO_2 @Pd NCs and 3.88978 ± 0.00008 Å for the Pd NCs, suggesting the absence of an alloyed PdSn phase (see Figure S1). The volume-averaged coherence lengths of the Pd NCs and the SnO_2 @Pd NCs were determined to be 21.26 ± 0.17 nm and 20.0 ± 0.2 nm, respectively.

Figures 1b and 1c display high-resolution TEM images of a SnO_2 @Pd NC and a Pd NC supported on carbon, respectively, showing a structural periodicity of 1.97 Å for both catalysts, which is in good agreement with the (200) of fcc Pd. The

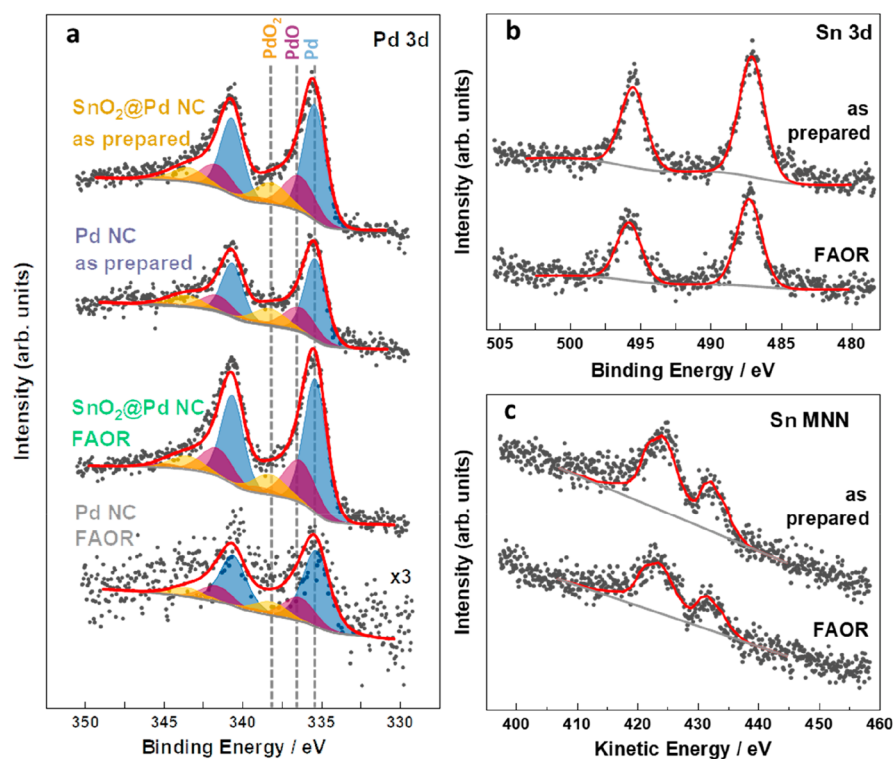


Figure 3. Quasi in situ XPS spectra for (a) Pd 3d core level of the Pd NCs and SnO₂@Pd NCs in the as-prepared state and after 1 h FAOR at 0.45 V in 0.1 M HClO₄. (b) Sn 3d XPS peaks and (c) Sn MNN AES peaks for the SnO₂@Pd NCs in the as-prepared state and after FAOR.

SnO₂@Pd NC additionally shows crystalline structures on top of the Pd NCs with 3.43 Å periodicity, corresponding to the (110) spacings of the rutile SnO₂ structure. The SnO₂ structures have a size of ~2 nm.

Figures 2a and 2b show HAADF-STEM images of uniformly shaped NCs in both samples, suggesting a high density of {100} facets in the as-prepared state. The EDX elemental mapping of the SnO₂@Pd NCs in Figure 2c demonstrates that Sn covers the Pd NCs, forming an incomplete shell. The average particle sizes (estimated edge length of the cubes) are 22 ± 4 nm for the Pd NCs and 21 ± 7 nm for the SnO₂@Pd NCs, and these values indicate a symmetric size and shape distribution. The reported error is the standard deviation. The latter sample has a SnO₂ shell ~2 nm thick, which contributes to the overall cube size. The distributions of the as-prepared NCs on the carbon support for both samples are shown in Figure S2. The Pd loading on carbon determined by ICP-MS was 7.2 wt % for the Pd NCs and 5.2 wt % for the SnO₂@Pd NCs, with 0.3 wt % Sn. After 3 h FAOR, neither Pd nor Sn from the catalysts were detectable in the electrolyte, which indicates a stable ratio between Pd and Sn for the SnO₂@Pd NCs. The overall atomic ratio determined by EDX is 96:4 for Pd:Sn, which is comparable to the Pd:Sn ratio of 94:6 determined by ICP-MS.

Prior to the electrocatalytic investigation, the catalysts were electrochemically activated by running 10 cycles between 0.1 V and 0.7 V in 0.1 M HClO₄. The STEM images and EDX mapping of the SnO₂@Pd NCs after the activation process, shown in Figure S3, reveal that the cubic structure is maintained, with a slightly smaller average size of 19 ± 4 nm, and only a negligible fraction of Sn lost (1%). Interestingly, the cubic morphology of Pd was also mostly preserved after cycling in formic acid up to 0.95 V for 20 cycles (see Figures 2d–f), as well as after 3 h of chronoamperometry

at 0.45 V (see Figures 2g–i). However, constant reaction conditions for 3 h seem to be less harmful (Figures 2g–i), while cycling the catalysts in formic acid leads to a deterioration of the NC shape for both catalysts (Figures 2d–f). The upper potential limit of 0.95 V during cycling induced Pd oxide formation, leading to the dissolution of Pd which can explain the morphological changes.^{49–51} Remarkably, the EDX maps show the growth of the uniformly distributed SnO₂ particles from ~2 nm in size to SnO_x agglomerations of up to 8 nm after FAOR. The STEM/EDX data also indicate that SnO₂ may dissolve, to some extent, from the Pd NC surface during the reaction. After 3 h of reaction at 0.45 V, the EDX ratio for Pd:Sn is 98:2, which is similar to that obtained after cycling in formic acid (99:1). A scheme in Figure 2j illustrates the evolution of the SnO₂@Pd nanocubes from a homogeneously distributed SnO₂ shell around the Pd NC to the formation of SnO₂ agglomerates on Pd after reaction.

3.2. Quasi In Situ XPS and Operando XAFS Characterization. To further understand the role of the surface composition and chemical state of Pd and Sn, quasi in situ XPS and operando XAFS measurements have been conducted. Figure 3a displays the XPS spectra of the Pd 3d core level of both catalysts in the as-prepared state and after 1 h of FAOR at 0.45 V with a direct transfer from the electrochemical cell into UHV without exposure to air. Note that our XPS data were not acquired in situ, but quasi in situ, which is a terminology employed to signify that the samples were never exposed to air during the transfer from the electrochemical cell to the UHV-XPS analysis system. Nevertheless, a major limitation of this method must be considered, which is the fact that the XPS data are not acquired under potential control. The spectra are deconvoluted in three doublets with 3d_{5/2} peaks at E_B = 335.2 eV, E_B = 336.3 eV, and E_B = 338.1 eV, corresponding to Pd,

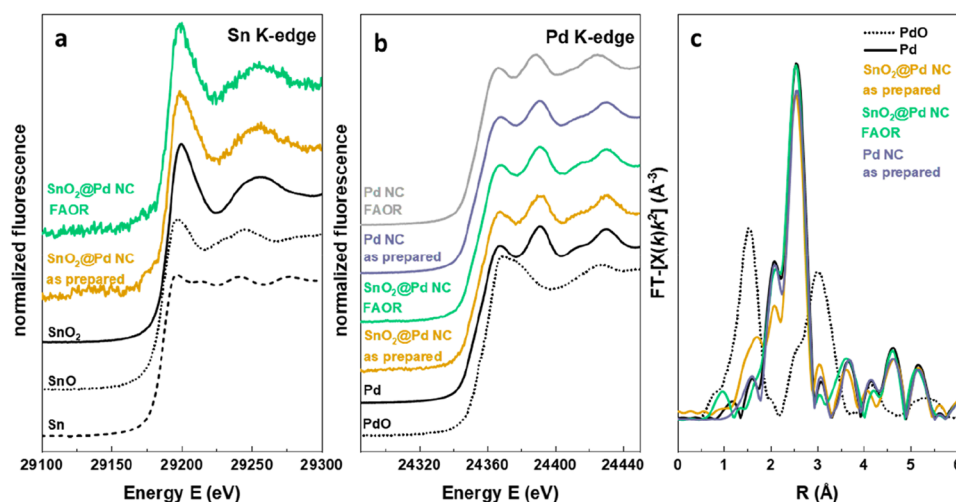


Figure 4. XANES spectra at the (a) Sn K-edge of SnO_2 @Pd NCs and (b) Pd K-edge for the Pd NCs, as well as SnO_2 @Pd NCs in the as-prepared state and operando spectra collected during 3 h of the FAOR in 0.1 M HClO_4 + 0.5 M HCOOH at 0.45 V vs. RHE. (c) Fourier-transformed (FT) k^2 -weighted Pd K-edge EXAFS spectra for both catalysts in the as-prepared state and during reaction. Reference spectra for bulk Sn, SnO, SnO_2 , Pd, and PdO are shown for comparison.

PdO, and PdO₂, respectively.⁵² Both catalysts show, besides the main Pd metal peak, small amounts of PdO and PdO₂ in the as-prepared state.^{53,54} Residues of the ligands and the ligand-removing agent were not observed in our as-prepared samples, as demonstrated by the absence of the Cl 2p, Br 3d, and Na 1s peaks in the XPS spectra (see Figure S4 in the Supporting Information). After reaction, and without sample exposure to air, it is observed that the Pd component of both catalysts, SnO_2 @Pd NCs and Pd NCs, remains partially oxidized. Our XPS results do not indicate the intermixing of Pd and SnO₂ and the formation of an interfacial PdSn alloy.

The Sn 3d spectra (see Figure 3b) were fitted with a spin-orbit doublet ($3d_{5/2}$ and $3d_{3/2}$), corresponding to SnO_x at $E_B = 487.0$ eV ($3d_{5/2}$).⁵⁵ Furthermore, the analysis of the Sn MNN Auger spectra was used to verify the Sn⁴⁺ oxidation state. Figure 3c depicts the Auger spectra of the SnO_2 @Pd NCs in the as-prepared state and after FAOR at 0.45 V. Both spectra were fitted with a SnO_2 reference spectrum. The data reveal a 4+ oxidation state of Sn in the as-prepared state, as well as after the activation process and after FAOR.

The surface Pd/Sn atomic ratio was quantified from the spectral area of the Pd and Sn 3d XPS peaks. The estimated Pd:Sn atomic ratio for the SnO_2 @Pd catalyst is 75:25 (XPS). A comparison of the Pd and Sn contents extracted from EDX and XPS data after the different sample treatments is shown in Table S1 in the Supporting Information. After reaction, the Pd:Sn surface ratio changes to 83:17, indicating an 8% loss of Sn at the surface. Thus, the distribution of SnO_2 on the Pd NC surface changes significantly toward a lower surface area of Sn, which indicates the formation of larger SnO_2 NP-like structures during the electrochemical reaction. Furthermore, when comparing the Pd-3d signal intensity of the bimetallic and monometallic samples, it is clear that the Pd NCs suffer from drastic material loss during the reaction, which was not observed for the SnO_2 @Pd NCs that appear to be stabilized by the presence of SnO_2 .

Complementary to the surface-sensitive XPS data, operando XAFS measurements were employed to probe the chemical state and structure in the bulk of the catalysts. The Pd K-edge data shown in Figure 4b, as well as Figure S4 in the Supporting

Information, demonstrate that the Pd species are in a reduced state and with a local environment similar to that in metallic fcc-Pd, both in the Pd NCs and in the SnO_2 @Pd NCs as-prepared catalysts. The Pd oxidation state and local structure also do not change under the reaction conditions. XANES analysis at the Sn K-edge (Figure 4a) confirms that the oxidation state and local structure around Sn in the SnO_2 @Pd NC catalyst is similar to that observed in the SnO_2 reference material, and does not change significantly during the reaction. Figure 4c depicts the Fourier-transform extended X-ray absorption fine structure (FT-EXAFS) spectra for the Pd K-edge. In agreement with the XANES data analysis, the EXAFS analysis shows that the as-prepared catalyst, as well as the catalyst during reaction, are in the reduced state, with a local structure similar to that of pure metallic Pd. The fitted EXAFS spectra and the structural parameters are shown in Figure S5 and Table S2 in the Supporting Information.

3.3. Electrochemical Analysis. For the electrochemical characterization of the catalysts, a sulfuric acid containing electrolyte was chosen since the specific adsorption of sulfates leads to a defined profile of the hydrogen adsorption/desorption region.^{56,57} The voltammetric profiles of the catalysts after 10 cycles in Figure S6(a) in the Supporting Information show peaks at 0.22 and 0.29 V for Pd NCs, which are associated with hydrogen adsorption/desorption on long {100} domains,¹⁸ confirming the cubic shape. The SnO_2 @Pd NC catalyst features a shifted hydrogen desorption peak at 0.27 V, indicating a distorted catalyst surface that is due to the presence of the second metal.

Prior to every FAOR reaction, an electrochemical pretreatment was performed by cycling the catalysts 10 times in the 0.1 M HClO_4 electrolyte. The FAOR measurements, as well as the CO-stripping experiments, were performed in 0.1 M HClO_4 because higher current densities are obtained, compared to the often-used 0.5 M H_2SO_4 .^{18,56,58,59} The specific adsorption of bisulfate at oxidative potentials blocks the active sites on Pd, which, hence, are not active for FAOR.^{12,60,61}

CO-stripping experiments were used to evaluate the CO tolerance of the catalysts. Under potential control, with the

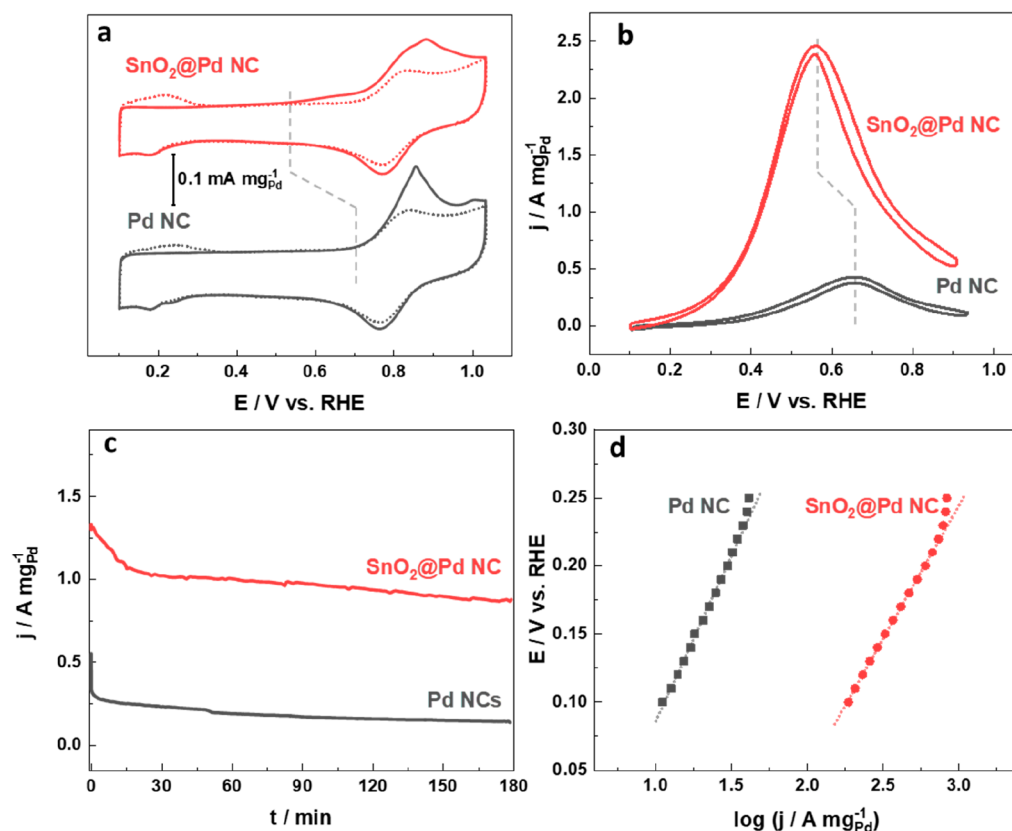


Figure 5. (a) CO-stripping voltammograms (solid lines) and subsequent cyclic voltammetry (dotted lines) of SnO₂@Pd catalysts (red) and Pd catalysts (gray) in 0.1 M HClO₄ at 20 mV s⁻¹. (b) Voltammetric profiles of the SnO₂@Pd NC (red) and Pd NC (gray) in 0.1 M HClO₄ + 0.5 M HCOOH at 50 mV s⁻¹. (c) Chronoamperometric curves of the SnO₂@Pd NC (red) and Pd NC (gray) at 0.45 V. (d) Tafel plots for SnO₂@Pd NCs (red) and Pd NCs (gray).

electrode at 0.1 V, CO was adsorbed on Pd such that the characteristic H_{Ads/Des} peaks were suppressed as shown in Figure 5a. The adsorbed CO was completely oxidized through a single cycle up to 1.0 V and the H_{Ads/Des} peaks reappeared subsequently in the second cycle. The similar peak potentials of both catalysts (0.86 V) indicate a mainly constant CO binding strength for both catalysts and, hence, no strain effect of the SnO₂ on the Pd lattice. However, the onset potential for CO oxidation was found to be reduced from 0.73 V for Pd NCs to 0.61 V for SnO₂@Pd NCs, as indicated by the gray dashed line. This result is in accordance with reports for non-shape-selected Pd and PdSn samples, where Sn-containing samples exhibited a 50–100 mV lower onset potential, because of the oxophilic sites providing oxygen at lower Sn oxidation potentials.^{29–34} The lower onset potential is accompanied by a slightly elevated oxidative current in a broad potential range, suggesting a more facile CO oxidation on Pd during this potential span. The broader CO oxidation peak of the SnO₂@Pd NCs suggests surface heterogeneity and a slower CO surface diffusion toward the reactive Pd sites in the presence of Sn. Thus, the presence of Sn atoms appears to facilitate the oxidative removal of CO.

The electrocatalytic activities of Pd NCs and SnO₂@Pd NCs for FAOR were characterized by cyclic voltammetry in 0.1 M HClO₄ + 0.5 M HCOOH between 0.1 V and 0.95 V at 50 mV s⁻¹ (Figure 5b). The currents were normalized to the amount of Pd obtained by ICP-MS, thus reporting mass activities. The specific activities, where voltammetric profiles are normalized by the electrochemical surface area calculated by CO stripping,

are reported in Table S3 and Figures S6(b) and S6(c) in the Supporting Information. A comparison of the ECSA calculated from CO oxidation and the H_{Ads/Des} is displayed in Table S3, with larger CO-stripping normalization, compared to the H_{Ads/Des}.⁶² The FAOR peak potential for our Pd NCs occurs at 0.65 V, which agrees well with the finding of Vidal-Iglesias et al. for unsupported Pd NCs under similar reaction conditions.¹⁸ Remarkably, the peak potential for SnO₂@Pd NCs shifts by 100 mV to a lower potential of 0.55 V, and they show a 5.8-fold increase of the current density at this potential, compared to the Pd NCs. A comparison of our catalysts with PdSn systems from the literature is shown in Table S4 in the Supporting Information, demonstrating the excellent performance of our catalysts. The higher FAOR current and the lower onset potential of our SnO₂@Pd NCs highlight the beneficial effect of SnO₂ for the enhancement of the catalytic activity.

Chronoamperometric curves for FAOR at different potentials were performed to test the CO poisoning rate and stability of the samples under reaction conditions (see Figure 5c, as well as Figure S6(c) in the Supporting Information). At 0.45 V, the current densities decrease slowly for both catalysts over a period of 3 h. However, the stationary currents for SnO₂@Pd NCs are 5.8 times higher, compared to Pd NCs. Thus, high catalytic activity and stability of our materials is obtained for the SnO₂@Pd NCs at 0.45 V.

Figure 5d displays the Tafel plots for FAOR, which were obtained from linear sweep voltammograms measured in quasi-steady state at 1 mV s⁻¹. The lower overpotential region between 0.1 V and 0.25 V displays a linear Tafel relationship

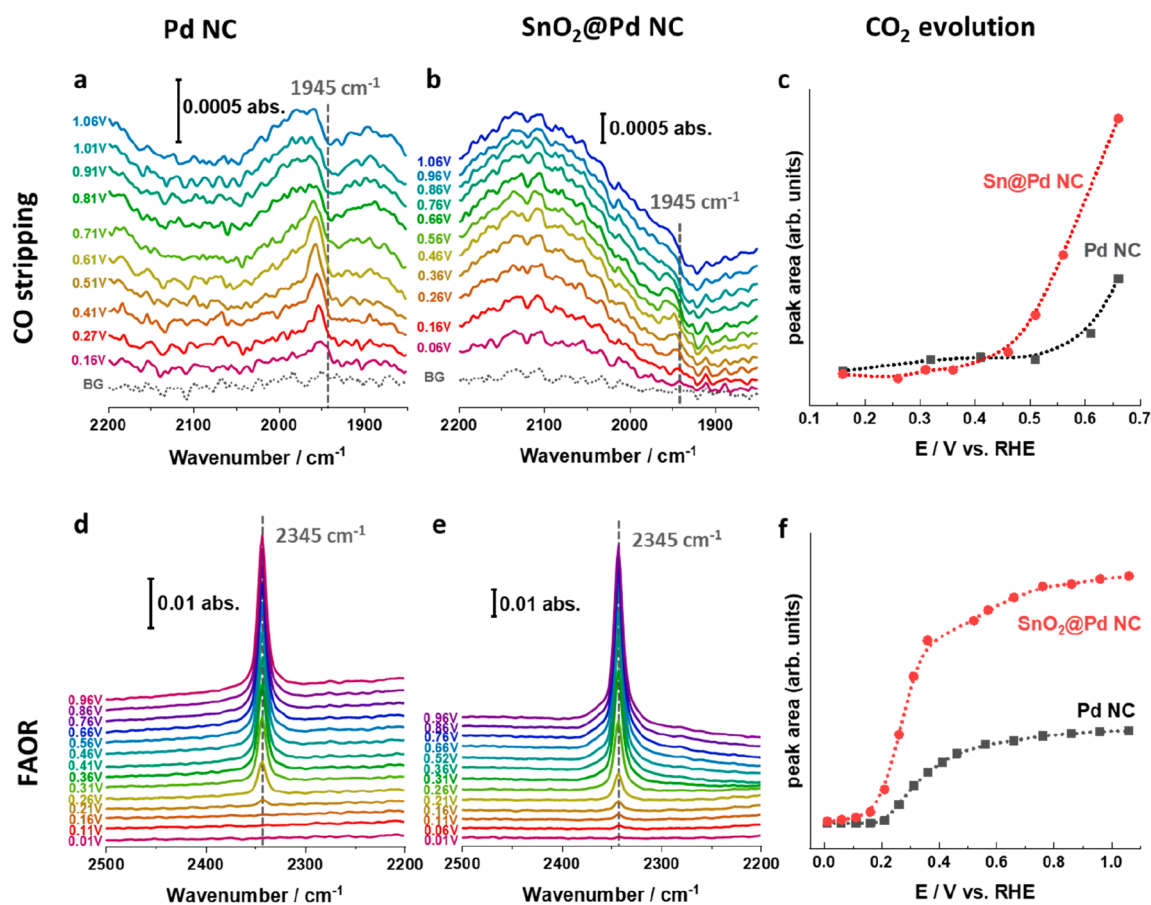


Figure 6. In situ FTIR of the CO-stripping experiments in the CO regime of (a) Pd NCs and (b) SnO₂@Pd NCs; (c) depicts the integrated intensities of the corresponding CO₂ bands. Reference spectra taken at 0.06 V vs. RHE, spectra taken on Au foil in 0.1 M HClO₄. In situ FTIR of FAOR show CO₂ bands during FAOR for (d) Pd NCs and (e) SnO₂@Pd NCs, while panel (f) depicts the integrated band intensities of the CO₂ bands during FAOR. Reference spectra taken at -0.04 V vs. RHE. Spectra taken on glassy carbon in 0.1 M HClO₄ and 25 mM HCOOH.

indicating a kinetically controlled regime of the reaction. A lower Tafel slope was obtained for SnO₂@Pd NCs (196 ± 6 mV dec⁻¹), compared to Pd NCs (247 ± 15 mV dec⁻¹), suggesting faster electrokinetics of the SnO₂-containing catalyst. The high Tafel slopes indicate that mass-transfer kinetics must be involved in the reaction process. Similar Tafel slopes have been reported for Pd catalysts for FAOR.⁶³ A second Tafel slope at higher potentials, as shown in Figure S6(d) in the Supporting Information, suggests strong mass-transfer limitations. The exchange current densities (j_0) were further calculated to demonstrate the particular portion of the electrode kinetics and the intrinsic catalytic activity. As the standard potential for FAOR, an E° (HCOOH/CO₂, H⁺) value of -0.19 V vs. RHE (-0.25 V vs. SHE) at 298 K was used.⁶⁴ Promoting Pd cubes with Sn appears to be very effective for boosting the catalytic activity, since SnO₂@Pd NCs resulted in a j_0 value of 0.96 mA cm⁻², compared to Pd NCs with 0.44 mA cm⁻². The order of magnitude is in a similar range to values for Pd reported in the literature.^{65–67} Thus, this result confirms the improved catalytic activity of SnO₂@Pd NCs, mainly because of its enhanced electrokinetics.

3.4. Spectro-electrochemical Measurements. The effect of the SnO₂ on the CO adsorption on SnO₂@Pd NCs was studied in situ via CO stripping by applying FTIR. For these experiments, the carbon-supported NCs were deposited

on an Au foil to enhance the reflectance of the IR light, while being inert for CO adsorption at room temperature. Hence, the electrode was pressed on the CaF₂ window after CO adsorption under potential control. The background spectrum was recorded at 0.06 V, then the potential was swept to positive values and held at the acquisition potential. With this configuration, negative bands indicate a disappearance of adsorbed species, while the species being formed appear as positive bands.⁶⁸ CO_{ads} features on Pd and Pt are usually influenced by an electrochemical Stark effect, leading to a potential-dependent wavenumber shift of the adsorbates.^{68–70} The position of the center of the CO band increases in wavenumber with applied potential, because of the perturbation of the vibrational frequency in the static electric field of the double layer. Potential-dependent peaks are shown at 1945 cm⁻¹ (see Figures 6a and 6b) and 2345 cm⁻¹ (see Figures S7(a) and S7(b)). The first one can be assigned to the bridge-bonded CO (C–O stretch; $\nu(\text{CO}_B) = 1900\text{--}1955$ cm⁻¹), and the latter one can be assigned to dissolved CO₂ (asymmetric C–O stretch; $\nu(\text{CO}_2) = 2345$ cm⁻¹).⁷ The acquired spectra show relatively weak CO bands, which can be attributed to the low catalyst loading on the carbon support. For the Pd NCs (Figure 6a), a CO_B band appears at 1945 cm⁻¹, which shifts from 1951 cm⁻¹ (0.16 V) to 1958 cm⁻¹ (0.71 V) and decreases starting from 0.71 V. Similar bands for SnO₂@Pd NCs start to shift in the same manner at 0.16 V from 1951 cm⁻¹, but the

peak intensity decreases already at 0.66 V. A negative band remains at 1945 cm^{-1} at higher potentials. These results are similar to the onset potentials observed in the electrochemical CO-stripping experiments and support the earlier CO oxidation of the SnO_2 @Pd NCs.

Figure S7 in the Supporting Information depicts the CO_2 evolution from the CO-stripping experiments for Pd NC and SnO_2 @Pd NC at 2345 cm^{-1} , respectively. The potential dependence of the integrated band intensities of the CO_2 formation are displayed in Figure 6c. While the onset potential for Pd NCs is observed at 0.71 V, CO_2 evolution starts 100 mV lower, at 0.66 V, for the SnO_2 @Pd NCs. The results from the in situ FTIR measurements are in good agreement with the CO_2 evolution of the CO-stripping experiments (0.73 V for Pd NCs and 0.61 V for SnO_2 @Pd NCs). Thus, we could show a weaker bond of CO to Pd when SnO_2 is present.

Furthermore, FAOR was followed using in situ FTIR by monitoring the CO_2 evolution. Figures 6d and 6e show the respective potential-dependent CO_2 evolution for Pd NCs and SnO_2 @Pd NCs, respectively. Glassy carbon was chosen as a substrate for the catalysts in these measurements, for better comparison with the catalytic investigation. No CO adsorption was observed in this experiment, which can be assigned to the low intrinsic adsorption of CO on Pd while sweeping the potential up. It is expected that significant amounts of adsorbed CO and formate only form after exposure to the oxidizing potentials for an extended period of time. The background was taken at -0.04 V after the immersion of the electrode into the 0.1 M HClO_4 + 25 mM HCOOH solution to avoid the spontaneous FAOR and ensure that we have a metallic Pd surface. The low formic acid concentration was chosen to reduce massive CO_2 bubble formation and to increase the sensitivity for the onset potential of CO_2 formation. For Pd NCs, CO_2 generation by formic acid decomposition starts to evolve at 0.21 V, while for the SnO_2 @Pd NCs, small amounts of CO_2 are already seen at 0.01 V, Figure 6f. The onset potentials for the catalytic activities measured by CV are 0.35 V (Pd NC) and 0.15 V (SnO_2 @Pd NC), which are both 140 mV higher than the onset potentials observed by FTIR, which again could be assigned to the higher sensitivity of the latter technique and to the intrinsic decomposition of formic acid. These results demonstrate a significant enhancement of the catalytic activity of SnO_2 @Pd NC already at low potentials.

The high catalytic performance of SnO_2 @Pd NCs, which exceeds that of the current catalysts in the literature (Table S4 in the Supporting Information), originates from the presence of SnO_2 close to the {100} facets of Pd NCs. CO-stripping experiments and their corresponding in situ FTIR revealed a decreased oxidizing potential of adsorbed CO, because of the presence of SnO_2 . The role of SnO_2 on the removal of poisoning CO is demonstrated. In this study, the enhanced FAOR performance is linked to the exclusive presence of SnO_2 on Pd in a segregated way, without the formation of a PdSn alloy. However, the role of the third-body effect and the diminution of unfavorable CO_{ads} formation through adatoms or steric hindrance cannot be excluded. The calculation of the electrochemical surface areas revealed a lower amount of active sites for SnO_2 @Pd NCs (see Table S3), which indicates a possible blockage of sites on which CO could bound. The presence of SnO_2 results in weaker bound CO_{ads} , which, in turn, can be oxidized at milder overpotentials, making Pd

active sites available for catalytic activity already at low overpotentials.

4. CONCLUSION

In the present “synthesis-by-design” approach, SnO_2 @Pd nanocubes and Pd nanocubes were prepared via a hydrothermal chemical synthesis, supported on carbon powder, and studied for the electrochemical oxidation of formic acid in an acidic medium. The system was chosen, because Pd NCs are expected to exhibit high catalytic performance due to the presence of {100} facets, while the existence of a second metal such as Sn is known to further enhance the activity through a bifunctional mechanism. The SnO_2 @Pd NCs presented here are the first non-alloyed Pd–Sn nanocube FAOR catalysts with an incomplete SnO_2 shell.

The presence of SnO_2 -like species on Pd was found to promote FAOR, which is linked to the oxidation of adsorbed CO at lower potentials as compared to Pd NCs. Since slow CO poisoning of the Pd surface leads to deactivation during FAOR, the presence of SnO_2 results in enhanced catalytic performance of SnO_2 @Pd NCs compared to bare Pd NCs. In particular, the SnO_2 @Pd NCs outperformed the Pd NCs, in terms of activity, with a 5.8-fold increase of current density with 2.5 $\text{A mg}_{\text{Pd}}^{-1}$ and a 100 mV lower peak potential. The catalytic properties also exceeded those of the known PdSn catalysts in the literature. However, the proposed catalyst is still prone to deactivation, to some extent. STEM and EDX, as well as quasi in situ XPS and operando XAS revealed that the shape, as well as the oxidation state, of the catalysts remained stable during and after reaction at 0.45 V. In situ FTIR studies confirmed the lower CO desorption potentials and lower overpotentials, as well as higher FAOR catalytic activities for SnO_2 @Pd NCs. In summary, our electrochemical and spectroscopic data suggest a bifunctional reaction mechanism in which SnO_2 promotes the oxidation of CO residues close to the Pd surface, improving the catalytic performance of Pd toward formic acid oxidation. Consequently, the SnO_2 @Pd NCs proposed here are promising candidates in order to achieve an optimum performance of formic acid fuel cells.

■ ASSOCIATED CONTENT

SI Supporting Information

The Supporting Information is available free of charge at <https://pubs.acs.org/doi/10.1021/acscatal.0c03212>.

XRD data refinements, complementary STEM images and histograms, comparison of Pd and Sn content extracted from TEM-EDX and XPS, EXAFS fitting details and results, electrochemical data normalized by CO-ECSA, comparison of electrochemical surface areas, comparison of electrocatalytic activities with other PdSn systems and complementary results for in situ FTIR (PDF)

■ AUTHOR INFORMATION

Corresponding Author

Beatriz Roldan Cuenya – Department of Interface Science, Fritz-Haber-Institute of the Max-Planck Society, 14195 Berlin, Germany; orcid.org/0000-0002-8025-307X; Email: roldan@fhi-berlin.mpg.de

Authors

Clara Rettenmaier – Department of Interface Science, Fritz-Haber-Institute of the Max-Planck Society, 14195 Berlin, Germany

Rosa M. Arán-Ais – Department of Interface Science, Fritz-Haber-Institute of the Max-Planck Society, 14195 Berlin, Germany; orcid.org/0000-0001-9892-1980

Janis Timoshenko – Department of Interface Science, Fritz-Haber-Institute of the Max-Planck Society, 14195 Berlin, Germany

Rubén Rizo – Department of Interface Science, Fritz-Haber-Institute of the Max-Planck Society, 14195 Berlin, Germany; orcid.org/0000-0001-8161-2989

Hyo Sang Jeon – Department of Interface Science, Fritz-Haber-Institute of the Max-Planck Society, 14195 Berlin, Germany

Stefanie Kühn – Department of Interface Science, Fritz-Haber-Institute of the Max-Planck Society, 14195 Berlin, Germany

See Wee Chee – Department of Interface Science, Fritz-Haber-Institute of the Max-Planck Society, 14195 Berlin, Germany

Arno Bergmann – Department of Interface Science, Fritz-Haber-Institute of the Max-Planck Society, 14195 Berlin, Germany

Complete contact information is available at:
<https://pubs.acs.org/10.1021/acscatal.0c03212>

Notes

The authors declare no competing financial interest.

ACKNOWLEDGMENTS

This work was supported by the European Research Council under Grant No. ERC-OPERANDOCAT (ERC-725915) and the Deutsche Forschungsgemeinschaft (DFG, German Research Foundation) under Germany's Excellence Strategy – EXC 2008–390540038 – UniSysCat. We acknowledge DESY (Hamburg, Germany), a member of the Helmholtz Association HGF, for the provision of experimental facilities. Portions of this research were performed at PETRA III, and we would like to thank Dr. Edmund Walter, for assistance in using the P65 beamline, and Dr. Vadim Murzin and Dr. Wolfgang Caliebe, for assistance in using the P64 beamline.

REFERENCES

- (1) Gong, Y.; Liu, X.; Gong, Y.; Wu, D.; Xu, B.; Bi, L.; Zhang, L. Y.; Zhao, X. S. Synthesis of defect-rich palladium-tin alloy nanochain networks for formic acid oxidation. *J. Colloid Interface Sci.* **2018**, *530* (15), 189–195.
- (2) Capon, A.; Parson, R. The oxidation of formic acid at noble metal electrodes: I. Review of previous work. *J. Electroanal. Chem. Interfacial Electrochem.* **1973**, *44* (1), 1–7.
- (3) Capon, A.; Parsons, R. The oxidation of formic acid at noble metal electrodes Part III. Intermediates and mechanism on platinum electrodes. *J. Electroanal. Chem. Interfacial Electrochem.* **1973**, *45* (2), 205–231.
- (4) Capon, A.; Parsons, R. The oxidation of formic acid on noble metal electrodes: II. A comparison of the behaviour of pure electrodes. *J. Electroanal. Chem. Interfacial Electrochem.* **1973**, *44* (2), 239–254.
- (5) Sun, D.; Si, L.; Fu, G.; Liu, C.; Sun, D.; Chen, Y.; Tang, Y.; Lu, T. Nanobranched porous palladium-tin intermetallics: One-step synthesis and their superior electrocatalysis towards formic acid oxidation. *J. Power Sources* **2015**, *280*, 141–146.
- (6) Grozovski, V.; Climent, V.; Herrero, E.; Feliu, J. M. Intrinsic activity and poisoning rate for HCOOH oxidation at Pt(100) and vicinal surfaces containing monoatomic (111) steps. *ChemPhysChem* **2009**, *10* (11), 1922–1926.
- (7) Miyake, H.; Okada, T.; Samjeské, G.; Osawa, M. Formic acid electrooxidation on Pd in acidic solutions studied by surface-enhanced infrared absorption spectroscopy. *Phys. Chem. Chem. Phys.* **2008**, *10* (25), 3662–3669.
- (8) Fayette, M.; Nutariya, J.; Vasiljevic, N.; Dimitrov, N. A study of Pt dissolution during formic acid oxidation. *ACS Catal.* **2013**, *3* (8), 1709–1718.
- (9) Jiang, K.; Zhang, H.-X.; Zou, S.; Cai, W.-B. Electrocatalysis of formic acid on palladium and platinum surfaces: from fundamental mechanisms to fuel cell applications. *Phys. Chem. Chem. Phys.* **2014**, *16* (38), 20360–20376.
- (10) Arenz, M.; Stamenkovic, V.; Ross, P. N.; Markovic, N. M. Surface (electro-)chemistry on Pt(111) modified by a Pseudomorphic Pd monolayer. *Surf. Sci.* **2004**, *573* (1), 57–66.
- (11) Arenz, M.; Stamenkovic, V.; Schmidt, T. J.; Wandelt, K.; Ross, P. N.; Markovic, N. M. The electro-oxidation of formic acid on Pt-Pd single crystal bimetallic surfaces. *Phys. Chem. Chem. Phys.* **2003**, *5* (19), 4242–4251.
- (12) Rizo, R.; Roldan Cuenya, B. Shape-Controlled Nanoparticles as Anodic Catalysts in Low-Temperature Fuel Cells. *ACS Energy Letters* **2019**, *4* (6), 1484–1495.
- (13) Yu, X.; Pickup, P. G. Mechanistic study of the deactivation of carbon supported Pd during formic acid oxidation. *Electrochem. Commun.* **2009**, *11* (10), 2012–2014.
- (14) Hoshi, N.; Kida, K.; Nakamura, M.; Nakada, M.; Osada, K. Structural effects of electrochemical oxidation of formic acid on single crystal electrodes of palladium. *J. Phys. Chem. B* **2006**, *110* (25), 12480–12484.
- (15) Baldauf, M.; Kolb, D. M. Formic acid oxidation on ultrathin Pd films on Au(*hkl*) and Pt(*hkl*) electrodes. *J. Phys. Chem.* **1996**, *100* (27), 11375–11381.
- (16) Zhang, X.; Yin, H.; Wang, J.; Chang, L.; Gao, Y.; Liu, W.; Tang, Z. Shape-dependent electrocatalytic activity of monodispersed palladium nanocrystals toward formic acid oxidation. *Nanoscale* **2013**, *5* (18), 8392–8397.
- (17) Jin, M.; Zhang, H.; Xie, Z.; Xia, Y. Palladium nanocrystals enclosed by {100} and {111} facets in controlled proportions and their catalytic activities for formic acid oxidation. *Energy Environ. Sci.* **2012**, *5* (4), 6352–6357.
- (18) Vidal-Iglesias, F. J.; Arán-Ais, R. M.; Solla-Gullón, J.; Garnier, E.; Herrero, E.; Aldaz, A.; Feliu, J. M. Shape-dependent electrocatalysis: Formic acid electrooxidation on cubic Pd nanoparticles. *Phys. Chem. Chem. Phys.* **2012**, *14* (29), 10258–10265.
- (19) Zheng, W.; Qu, J.; Hong, X.; Tedsree, K.; Tsang, S. C. E. Probing the Size and Shape Effects of Cubic- and Spherical-Shaped Palladium Nanoparticles in the Electrooxidation of Formic Acid. *ChemCatChem* **2015**, *7* (23), 3826–3831.
- (20) Solla-Gullón, J.; Montiel, V.; Aldaz, A.; Clavilier, J. Electrochemical and electrocatalytic behaviour of platinum-palladium nanoparticle alloys. *Electrochem. Commun.* **2002**, *4* (9), 716–721.
- (21) Zhang, S.; Shao, Y.; Yin, G.; Lin, Y. Electrostatic self-assembly of a Pt-around-Au nanocomposite with high activity towards formic acid oxidation. *Angew. Chem., Int. Ed.* **2010**, *49* (12), 2211–2214.
- (22) Liu, J.; Zheng, Y.; Hong, Z.; Cai, K.; Zhao, F.; Han, H. Microbial synthesis of highly dispersed PdAu alloy for enhanced electrocatalysis. *Sci. Adv.* **2016**, *2* (9), e1600858–e1600858.
- (23) Tang, Y.; Zou, S. Formic Acid Oxidation on Pd Thin Film Coated Au Nanocrystals. *Surfaces* **2019**, *2* (2), 372–386.
- (24) Xiao, X.; Jeong, H.; Song, J.; Ahn, J. P.; Kim, J.; Yu, T. Facile synthesis of Pd@Pt core-shell nanocubes with low Pt content: Via direct seed-mediated growth and their enhanced activity for formic acid oxidation. *Chem. Commun.* **2019**, *55* (79), 11952–11955.
- (25) Liu, D.; Xie, M.; Wang, C.; Liao, L.; Qiu, L.; Ma, J.; Huang, H.; Long, R.; Jiang, J.; Xiong, Y. Pd-Ag alloy hollow nanostructures with

interatomic charge polarization for enhanced electrocatalytic formic acid oxidation. *Nano Res.* **2016**, *9* (6), 1590–1599.

(26) Li, F.; Li, W.; Liu, H.; Liu, C.; Dong, G.; Liu, J.; Peng, K. Palladium Nanoparticles Loaded on TiO₂–Graphene Hybrids (Pd/TiO₂–Gr) with Enhanced Electrocatalytic Activity in Formic Acid Oxidation. *Russ. J. Phys. Chem. A* **2018**, *92* (8), 1550–1557.

(27) Jana, R.; Subbarao, U.; Peter, S. C. Ultrafast synthesis of flower-like ordered Pd₃Pb nanocrystals with superior electrocatalytic activities towards oxidation of formic acid and ethanol. *J. Power Sources* **2016**, *301*, 160–169.

(28) Liu, Z.; Fu, G.; Li, J.; Liu, Z.; Xu, L.; Sun, D.; Tang, Y. Facile synthesis based on novel carbon-supported cyanogel of structurally ordered Pd₃Fe/C as electrocatalyst for formic acid oxidation. *Nano Res.* **2018**, *11* (9), 4686–4696.

(29) Liu, Z.; Zhang, X. Carbon-supported PdSn nanoparticles as catalysts for formic acid oxidation. *Electrochem. Commun.* **2009**, *11* (8), 1667–1670.

(30) Tu, D.; Wu, B.; Wang, B.; Deng, C.; Gao, Y. A highly active carbon-supported PdSn catalyst for formic acid electrooxidation. *Appl. Catal., B* **2011**, *103* (1–2), 163–168.

(31) Wang, H.; Liu, Z.; Ma, Y.; Julian, K.; Ji, S.; Linkov, V.; Wang, R. Synthesis of carbon-supported PdSn–SnO₂ nanoparticles with different degrees of interfacial contact and enhanced catalytic activities for formic acid oxidation. *Phys. Chem. Chem. Phys.* **2013**, *15* (33), 13999–14005.

(32) Lu, H.; Fan, Y.; Huang, P.; Xu, D. SnO₂ nanospheres supported Pd catalyst with enhanced performance for formic acid oxidation. *J. Power Sources* **2012**, *215*, 48–52.

(33) Feng, Y.; Bin, D.; Zhang, K.; Ren, F.; Wang, J.; Du, Y. One-step synthesis of nitrogen-doped graphene supported PdSn bimetallic catalysts for ethanol oxidation in alkaline media. *RSC Adv.* **2016**, *6* (23), 19314–19321.

(34) Hung, W. Z.; Chung, W. H.; Tsai, D. S.; Wilkinson, D. P.; Huang, Y. S. CO tolerance and catalytic activity of Pt/Sn/SnO₂ nanowires loaded on a carbon paper. *Electrochim. Acta* **2010**, *55* (6), 2116–2122.

(35) Wang, R. X.; Fan, Y. J.; Liang, Z. R.; Zhang, J. M.; Zhou, Z. Y.; Sun, S. G. PdSn nanocatalysts supported on carbon nanotubes synthesized in deep eutectic solvents with high activity for formic acid electrooxidation. *RSC Adv.* **2016**, *6* (65), 60400–60406.

(36) Qin, Q.; Xie, J.; Dong, Q.; Yu, G.; Chen, H. Surfactant-free fabrication of porous PdSn alloy networks by self-assembly as superior freestanding electrocatalysts for formic acid oxidation. *New J. Chem.* **2019**, *43* (48), 19242–19252.

(37) Rizo, R.; Arán-Ais, R. M.; Padgett, E.; Muller, D. A.; Lázaro, M. J.; Solla-Gullón, J.; Feliu, J. M.; Pastor, E.; Abruña, H. D. Pt-Richcore/Sn-Richsurface/Pt-skin Nanocubes As Highly Active and Stable Electrocatalysts for the Ethanol Oxidation Reaction. *J. Am. Chem. Soc.* **2018**, *140* (10), 3791–3797.

(38) Antolini, E.; Gonzalez, E. R. Effect of synthesis method and structural characteristics of Pt–Sn fuel cell catalysts on the electro-oxidation of CH₃OH and CH₃CH₂OH in acid medium. *Catal. Today* **2011**, *160* (1), 28–38.

(39) Liu, H. X.; Tian, N.; Brandon, M. P.; Pei, J.; Huangfu, Z. C.; Zhan, C.; Zhou, Z. Y.; Hardacre, C.; Lin, W. F.; Sun, S. G. Enhancing the activity and tuning the mechanism of formic acid oxidation at tetrahedral Pt nanocrystals by Au decoration. *Phys. Chem. Chem. Phys.* **2012**, *14* (47), 16415–16423.

(40) Shao, M. *Electrocatalysis in Fuel Cells A Non-and Low-Platinum Approach*. Springer–Verlag: London, 2013; pp 43–67.

(41) Wang, J. Y.; Zhang, H. X.; Jiang, K.; Cai, W. B. From HCOOH to CO at Pd electrodes: A surface-enhanced infrared spectroscopy study. *J. Am. Chem. Soc.* **2011**, *133* (38), 14876–14879.

(42) Zhang, H. X.; Wang, S. H.; Jiang, K.; André, T.; Cai, W. B. In situ spectroscopic investigation of CO accumulation and poisoning on Pd black surfaces in concentrated HCOOH. *J. Power Sources* **2012**, *199*, 165–169.

(43) Obradović, M. D.; Gojković, S. L. HCOOH oxidation on thin Pd layers on Au: Self-poisoning by the subsequent reaction of the reaction product. *Electrochim. Acta* **2013**, *88*, 384–389.

(44) Gasteiger, H. A.; Kocha, S. S.; Sompalli, B.; Wagner, F. T. *Appl. Catal., B* **2005**, *56*, 9–35.

(45) Mayrhofer, K. J. J.; Strmcnik, D.; Blizanac, B. B.; Stamenkovic, V.; Arenz, M.; Markovic, N. M. Measurement of oxygen reduction activities via the rotating disc electrode method: From Pt model surfaces to carbon-supported high surface area catalysts. *Electrochim. Acta* **2008**, *53* (7), 3181–3188.

(46) Momma, K.; Izumi, F. VESTA 3 for three-dimensional visualization of crystal, volumetric and morphology data. *J. Appl. Crystallogr.* **2011**, *44* (6), 1272–1276.

(47) Leonard, N.; Ju, W.; Sinev, I.; Steinberg, J.; Luo, F.; Varela, A. S.; Roldan Cuenya, B.; Strasser, P. The chemical identity, state and structure of catalytically active centers during the electrochemical CO₂ reduction on porous Fe–nitrogen–carbon (Fe–N–C) materials. *Chemical Science* **2018**, *9* (22), 5064–5073.

(48) Ravel, B.; Newville, M. ATHENA, ARTEMIS, HEPHAESTUS: Data analysis for X-ray absorption spectroscopy using IFEFFIT. *J. Synchrotron Radiat.* **2005**, *12* (4), 537–541.

(49) Myers, D. J.; Wang, X.; Smith, M. C.; More, K. L. Potentiostatic and Potential Cycling Dissolution of Polycrystalline Platinum and Platinum Nano-Particle Fuel Cell Catalysts. *J. Electrochem. Soc.* **2018**, *165* (6), F3178–F3190.

(50) Yasuda, K.; Taniguchi, A.; Akita, T.; Ioroi, T.; Siroma, Z. Platinum dissolution and deposition in the polymer electrolyte membrane of a PEM fuel cell as studied by potential cycling. *Phys. Chem. Chem. Phys.* **2006**, *8* (6), 746–752.

(51) Burke, L. D.; Casey, J. K. An Examination of the Electrochemical Behavior of Palladium in Base. *J. Electrochem. Soc.* **1993**, *140* (5), 1292–1298.

(52) Kibis, L. S.; Titkov, A. I.; Stadnichenko, A. I.; Koscheev, S. V.; Boronin, A. I. X-ray photoelectron spectroscopy study of Pd oxidation by RF discharge in oxygen. *Appl. Surf. Sci.* **2009**, *255* (22), 9248–9254.

(53) Kappler, J.; Bârsan, N.; Weimar, U.; Diéguez, A.; Alay, J. L.; Romano-Rodríguez, A.; Morante, J. R.; Göpel, W. Correlation between XPS, Raman and TEM measurements and the gas sensitivity of Pt and Pd doped SnO₂ based gas sensors. *Fresenius' J. Anal. Chem.* **1998**, *361* (2), 110–114.

(54) Domashevskaya, E. P.; Ryabtsev, S. V.; Turishchev, S. Yu.; Kashkarov, V. M.; Yurakov, Y. A.; Chuvankova, O. A.; Shchukarev, A. V. XPS and XANES Studies of SnOx Nanolayers. *J. Struct. Chem.* **2008**, *49*, 80–91.

(55) Stranick, M. A.; Moskwa, A. SnO₂ by XPS. *Surf. Sci. Spectra* **1993**, *2* (1), 50–54.

(56) Hoshi, N.; Kuroda, M.; Hori, Y. Voltammograms of stepped and kinked stepped surfaces of palladium: Pd(S)-[n(111)×(100)] and Pd(S)-[n(100)×(110)]. *J. Electroanal. Chem.* **2002**, *521* (1–2), 155–160.

(57) Vidal-Iglesias, F. J.; Arán-Ais, R. M.; Solla-Gullón, J.; Herrero, E.; Feliu, J. M. Electrochemical Characterization of Shape-Controlled Pt Nanoparticles in Different Supporting Electrolytes. *ACS Catal.* **2012**, *2* (5), 901–910.

(58) Arán-Ais, R. M.; Vidal-Iglesias, F. J.; Solla-Gullón, J.; Herrero, E.; Feliu, J. M. Electrochemical Characterization of Clean Shape-Controlled Pt Nanoparticles Prepared in Presence of Oleylamine/Oleic Acid. *Electroanalysis* **2015**, *27* (4), 945–956.

(59) Hara, M.; Linke, U.; Wandlowski, T. Preparation and electrochemical characterization of palladium single crystal electrodes in 0.1 M H₂SO₄ and HClO₄. Part I. Low-index phases. *Electrochim. Acta* **2007**, *52* (18), 5733–5748.

(60) Ishikawa, Y.; Liao, M. S.; Cabrera, C. R. Oxidation of methanol on platinum, ruthenium and mixed Pt–M metals (M = Ru, Sn): A theoretical study. *Surf. Sci.* **2000**, *463* (1), 66–80.

(61) Arenz, M.; Mayrhofer, K. J. J.; Stamenkovic, V.; Blizanac, B. B.; Tomoyuki, T.; Ross, P. N.; Markovic, N. M. The Effect of the Particle

Size on the Kinetics of CO Electrooxidation on High Surface Area Pt Catalysts. *J. Am. Chem. Soc.* **2005**, *127* (18), 6819–6829.

(62) Rudi, S.; Cui, C. H.; Gan, L.; Strasser, P. Comparative Study of the Electrocatalytically Active Surface Areas (ECSAs) of Pt Alloy Nanoparticles Evaluated by H-upd and CO-stripping voltammetry. *Electrocatalysis* **2014**, *5* (4), 408–418.

(63) Uwitonze, N.; Zhou, D.; Lei, J.; Chen, W.; Zuo, X. Q.; Cai, J.; Chen, Y. X. The high Tafel slope and small potential dependence of activation energy for formic acid oxidation on a Pd electrode. *Electrochim. Acta* **2018**, *283* (1), 1213–1222.

(64) Garbarino, S.; Burke, L. D. The surface active site model for formic acid electrooxidation at palladium in aqueous acid solution. *Int. J. Electrochem. Sci.* **2010**, *5* (6), 828–851.

(65) Douk, A. S.; Saravani, H.; Farsadrooh, M. Three-dimensional inorganic polymer of Pd aerogel as a highly active support-less anode catalyst toward formic acid oxidation. *Int. J. Hydrogen Energy* **2019**, *44* (33), 18028–18037.

(66) Zhang, Z.; Gong, Y.; Wu, D.; Li, Z.; Li, Q.; Zheng, L.; Chen, W.; Yuan, W.; Zhang, L. Y. Facile fabrication of stable PdCu clusters uniformly decorated on graphene as an efficient electrocatalyst for formic acid oxidation. *Int. J. Hydrogen Energy* **2019**, *44* (5), 2731–2740.

(67) Romero Hernández, A.; Arce Estrada, E. M.; Ezeta, A.; Manríquez, M. E. Formic acid oxidation on AuPd core-shell electrocatalysts: Effect of surface electronic structure. *Electrochim. Acta* **2019**, *327* (10), 134977–134977.

(68) Lin, W. F.; Iwasita, T.; Vielstich, W. Catalysis of CO electrooxidation at Pt, Ru, and PtRu alloy. An in situ FTIR study. *J. Phys. Chem. B* **1999**, *103* (16), 3250–3257.

(69) Lambert, D. K. Electric field induced change of adsorbate vibrational line strength. *J. Chem. Phys.* **1991**, *94*, 6237–6242.

(70) Iwasita, T.; Nart, F. C. In situ infrared spectroscopy at electrochemical interfaces. *Prog. Surf. Sci.* **1997**, *55* (4), 271–340.